Mechanics of Materials 148 (2020) 103419

Contents lists available at ScienceDirect

Mechanics of Materials

journal homepage: www.elsevier.com/locate/mechmat

Accounting for Shear Anisotropy and Material Frame Rotation on the Constitutive Characterization of Automotive Alloys using Simple Shear Tests

A. Abedini*, J. Noder, C.P. Kohar, C. Butcher

Department of Mechanical and Mechatronics Engineering, University of Waterloo, Waterloo, ON, CANADA

ARTICLE INFO

Keywords:
Simple shear
Hardening behaviour
Anisotropy
Constitutive response
Dual-phase steel
Aluminum alloy

ABSTRACT

Simple shear tests are an increasingly attractive method to determine the equivalent stress-strain response of sheet metals. Unlike uniaxial tensile tests, shear tests can reveal the hardening behaviour of materials to large strains without stress state deviations triggered by tensile instability. However, there has been some uncertainty surrounding the interpretation of the shear response of anisotropic materials due to the definition of appropriate equivalent strain measures and the development of normal stresses. In the present study, the development of normal stresses during simple shear of anisotropic materials is analyzed and are found to be negligible relative to the magnitude of the applied shear stress. It is demonstrated that erroneous normal stresses may arise as a consequence of calibration of anisotropic yield functions. An experimental methodology was then proposed consisting of shear tests in multiple orientations to characterize shear anisotropy and account for rotation of the material frame on the hardening response. The methodology considers non-linear interpolation using either a calibrated yield function using both shear and tensile data or from a simplified phenomenological form calibrated using only the shear data. A range of automotive alloys were considered including DP980 and DP1180 advanced high strength steel alloys, an aluminum-magnesium alloy, AA5182-O, and an AA6063-T6 aluminum extrusion with severe anisotropy. It is demonstrated that for relatively isotropic materials such as the DP steels, accounting for material frame rotation results in an approximately 2% difference in the extracted hardening data compared to the case when the material rotation is neglected. This variation is expected to be within the experimental uncertainty. For materials with more pronounced anisotropy such as AA5182-O sheet and AA6063-T6 extrusions, the change in the hardening response is more significant and can reach up to 5% and 15%, respectively.

1. Introduction

Finite-element simulations of automotive alloys in metal forming processes and component performance evaluation rely upon the accurate characterization of the stress-strain response to large strains that are far beyond the achievable strains in uniaxial tensile tests before the onset of diffuse necking. To mitigate this issue, inverse techniques such as inverse finite-element analysis (e.g. Dunand and Mohr, 2010; Tardif and Kyriakides, 2012; Roth and Mohr, 2016; Abedini *et al.*, 2018a; Baral *et al.*, 2019; Ha *et al.*, 2019) and internal-to-external work balance techniques such as the virtual field methods (e.g. Coppieters *et al.*, 2011; Rossi *et al.*, 2018) have been utilized to extract flow curves beyond the diffuse necking strain in tensile tests. Deformation in uniaxial tensile tests is homogeneous and plane stress until the onset of diffuse necking when the stress state in the neck transitions towards a triaxial stress state of plane strain tension with severe local stress and strain gradients. Inverse finite-element techniques require precise 3-D anisotropic yield functions to capture the local necking process which is challenging to accurately calibrate due to the characterization tests for anisotropy of sheet metals often being restricted to plane stress. In particular, difficulties in the experimental characterization of the yield stress in plane strain tension leads to approximations (see Flores *et al.*, 2010) that add further uncertainty to inverse methods. Furthermore, the correlation of the "global" load-displacement from experimental measurements and predictions from simulations of tensile tests does not indicate that the correct hardening model has been determined. The predicted local neck dimensions at the minimum cross-section must also be validated (Tardif and Kyriakides, 2012).

Despite the relative popularity of inverse numerical approaches, the solutions are sensitive to the anisotropic yield function, strain rate, mesh size, and element formulation which can alter deformation within the neck and can be implicitly washed-out by altering the hardening

* Corresponding Author.
E-mail address: aabedini@uwaterloo.ca (A. Abedini).

https://doi.org/10.1016/j.mechmat.2020.103419
Received 7 September 2019; Received in revised form 4 February 2020; Accepted 7 April 2020
Available online 17 May 2020

model. Effectively, the errors and uncertainties in the finite-element model are compensated for in the hardening response which at least in theory, is a material constant and not a calibration parameter. Experimental approaches for constitutive characterization that avoid numerical simulations or *a priori* assumptions of the material behaviour remain of great interest to the automotive industry.

The hydraulic bulge test is perhaps the preferred experimental method to determine the hardening response of sheet metals to larger strain levels than in the uniaxial tensile test (Koc *et al.*, 2011). From the analysis of Hill (1950) using an isotropic power law hardening material with an exponent of "n", instability in a tensile test will occur when $\varepsilon_{eq} = \varepsilon_1 = n$ but is delayed until a much higher strain level of $\varepsilon_{eq} = 2\varepsilon_1 = 4(1 + 2n)/11$ in the bulge test. For low hardening materials, $n \approx 0$, the bulge test can provide the stress response until an equivalent strain of about 0.36 whereas the uniaxial tensile test will theoretically neck at the onset of yielding. Although the mechanics of spherical bulging of a membrane are well-suited for constitutive characterization, there are experimental challenges that need to be considered. Bending strains, die entry radii, and material anisotropy are unavoidable in the test and may affect the curvature of the bulge. Measurement of the curvature using stereo digital image correlation (DIC) including the assumed functional form for the spherical or ellipsoidal surface and its calibration from the spatial data can significantly influence the flow stress. Resolving the curvature of the sheet at lower strain levels is also challenging and provides a practical lower bound for the stress-strain response. It is worth mentioning that as pointed out by Mudler *et al.* (2015), the stress state in bulge tests of anisotropic materials lies between the bounds of equal biaxial stress and equal biaxial straining. A recent study by Min *et al.* (2017) provides a comprehensive methodology for the analysis of bulge tests and highlights the experimental details that must be taken into account. The complexities of the bulge test, along with requiring a specialized test frame, provide a barrier for many research labs.

Alternatively, the use of shear tests to determine the hardening behaviour of materials has been on the rise in recent years (Peirs *et al.*, 2012; Yin *et al.*, 2014; Muhammad *et al.*, 2017; Rahmaan *et al.*, 2017; Abedini *et al.*, 2017a, 2018b; Traphöner *et al.*, 2018) specifically after the advent of DIC techniques for full-field strain measurement. Before DIC, determination of local strains in the shear gauge region was challenging because unlike uniaxial tension, there is no intrinsic gauge length in shear tests. Simple shear tests can be conducted using standard tensile test frames but in contrast to tensile and bulge tests, shear tests do not suffer from tensile instability and provide a direct way of establishing the stress-strain response to large strain levels. The mechanics of simple shear ensures that deformation is both plane stress and plane strain without any through-thickness stress or strain gradients. Despite the considerable advantages of simple shear tests, there have been many debates in the literature surrounding the analysis of shear data and the selection of shear specimen geometry. The shear test geometry must provide homogeneous deformation within the gauge region with an incremental principal strain ratio of -1.0. Many promising designs have been proposed and discussed by Peirs *et al.* (2012), Yin *et al.* (2014), and Roth and Mohr (2018). Furthermore, the choice of objective rate and the appropriate definition for the work-conjugate equivalent strain for finite plastic deformation in shear have been recently addressed by Butcher and Abedini (2017). More recently, Abedini *et al.* (2018b) derived a physically-necessary constraint on plastic flow that must be enforced upon the pressure-independent plastic potential or yield function if the associated flow rule is assumed. If the so-called shear constraint is not enforced, a spurious non-zero hydrostatic stress or stress triaxiality will be predicted that may significantly alter the mechanical response and will influence the failure predictions using phenomenological damage models.

Rahmaan *et al.* (2017) utilized the mechanics of shear deformation to develop a novel technique to extract the hardening response of a DP600 steel and an AA5182-O aluminum alloy using a combination of tensile and shear tests. Using plastic work equivalence, the experimental shear-to-equivalent stress ratio was used to convert the shear stress versus plastic work data to a work-conjugate equivalent stress versus plastic strain. Noder and Butcher (2019) refined the methodology to first use the tensile data until the plastic work at the onset of diffuse necking to avoid uncertainty with initial inhomogeneous yielding of the shear specimen while the hardening curve at large strains was determined by shear data. A limitation of the methodologies of Rahmaan *et al.* (2017) and Noder and Butcher (2019) is that shear anisotropy was assumed to be marginal over the range of strain considered so that the shear-to-equivalent stress ratio remains constant despite rotation of the material frame. For materials with shear anisotropy, it was left to the analyst to determine an appropriate cut-off strain for the shear conversion based upon rotation of the material axes. Recently, Chen *et al.* (2018) performed a parametric study on the influence of rotation of the material frame on the hardening response obtained by torsion tests on AA6061-T6 tubes performed by Scales *et al.* (2016). The Hill48 yield function (Hill, 1948) was employed and calibrated to predict shear anisotropy to convert the shear stress to an equivalent stress, which was demonstrated to be important to consider in the analysis. The rotation of the material axes by Chen *et al.* (2018) was based upon the material spin using the vorticity tensor. Recently, Kohar *et al.* (2019a) proposed a method to account for the influence of the plastic spin on the material axes in phenomenological plasticity to improve the predicted material response in shear stress states.

The objective of the present work is to generalize the experimental methodology of Rahmaan *et al.* (2017) by accounting for shear anisotropy and the rotation of the material frame with deformation. The accuracy of anisotropic yield functions that are predominantly calibrated using tensile-based data to predict shear anisotropy when analyzing shear tests is uncertain and may introduce larger errors than assuming that the shear-to-equivalent stress ratio is constant over the range of deformation. Moreover, the development of normal stresses due to shear anisotropy and their interaction with an assumed yield criterion on the hardening response requires further investigation. To these ends, the formation of normal stresses and the influence of the rotation of the material axes of anisotropic materials will be studied in the present study from the perspective of mechanics of shear deformation. An experimental methodology is then proposed to employ shear tests at several orientations to account for shear anisotropy on the hardening response. A range of commercial automotive alloys with body centred cubic (BCC) and face centred cubic (FCC) crystal structures with varying degree of anisotropy are considered. The materials include two dual-phase (DP) advanced high strength steels with relatively mild anisotropy, DP980 and DP1180, an aluminum-magnesium alloy sheet, AA5182-O, and an AA6063-T6 extrusion with severe anisotropy. Hexagonal close packed (HCP) materials were intentionally excluded due to their strong tension-compression asymmetry and deformation mechanisms of slip and twinning that lead to the so-called Swift effects in shear (Swift, 1947). It will be shown that the material axes rotation in simple shear impacts the hardening response of the four automotive alloys with various degrees of severity.

2. Mechanics of Simple Shear

2.1. Strain State

The fundamentals of the mechanics of simple shear deformation are briefly reviewed in this section. The readers are referred to Butcher and Abedini (2017) for a more detailed description, including derivations of the equations presented in this section. An element undergoing simple shear deformation is shown in Figure 1. The deformation gradient, $\boldsymbol{F}$, is:

$$\boldsymbol{F} = \begin{bmatrix} 1 & \gamma & 0 \\ 0 & 1 & 0 \\ 0 & 0 & 1 \end{bmatrix} \quad , \gamma = \tan(\theta) \tag{1}$$

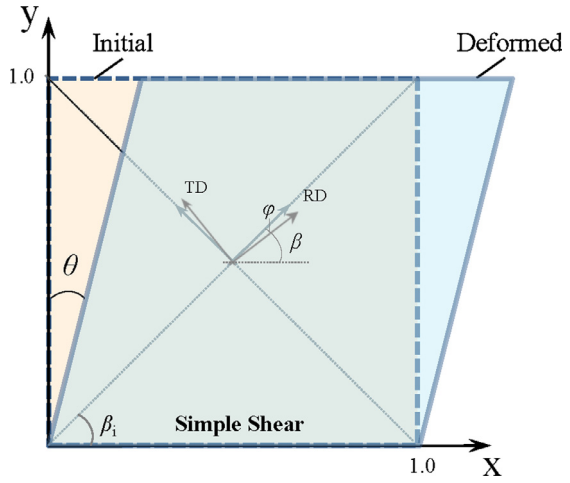

Figure. 1. An element is subject to simple shear deformation. The x-y is a global (fixed) frame. The RD-TD is the material frame that has been depicted schematically to show the rotation of the material axes.

Note that second-order tensors are designated using bold-face italicized letters such as ***F***, and fourth-order tensors as bold-face capital letters as in the elastic moduli tensor, $\mathbb{L}$.

The rate of deformation tensor, ***D***, and its principal strain increments (eigenvalues) in descending order are:

$$\boldsymbol{D} = sym(d\boldsymbol{F}\boldsymbol{F}^{-1}) = \begin{bmatrix} 0 & d\gamma/2 & 0 \\ d\gamma/2 & 0 & 0 \\ 0 & 0 & 0 \end{bmatrix}, \tag{2}$$

$$eig(\boldsymbol{D}) = \begin{bmatrix} D_1 \\ D_2 \\ D_3 \end{bmatrix} = \begin{bmatrix} d\gamma/2 \\ 0 \\ -d\gamma/2 \end{bmatrix} \tag{3}$$

and the vorticity tensor, ***W***, is:

$$\boldsymbol{W} = skewsym(d\boldsymbol{F}\boldsymbol{F}^{-1}) = \begin{bmatrix} 0 & d\gamma/2 & 0 \\ -d\gamma/2 & 0 & 0 \\ 0 & 0 & 0 \end{bmatrix} \tag{4}$$

The rate of deformation tensor, ***D***, is the objective rate of the logarithmic strain and is exactly integrable to the finite strain solution when using the logarithmic spin tensor (Xiao *et al.*, 1997). The total logarithmic strain and its principal values are:

$$\varepsilon = \frac{\sinh^{-1}(\gamma/2)}{\sqrt{4+\gamma^2}} \begin{bmatrix} \gamma & 2 & 0 \\ 2 & -\gamma & 0 \\ 0 & 0 & 0 \end{bmatrix}, \tag{5}$$

$$eig(\varepsilon) = \begin{bmatrix} \varepsilon_1 \\ \varepsilon_2 \\ \varepsilon_3 \end{bmatrix} = \begin{bmatrix} \sinh^{-1}(\gamma/2) \\ 0 \\ -\sinh^{-1}(\gamma/2) \end{bmatrix} \tag{6}$$

The orientation of the major principal strain is defined by the angle:

$$\alpha = \frac{1}{2}\tan^{-1}\left(\frac{2}{\gamma}\right) \tag{7}$$

and rotates with deformation from $\alpha = 45^\circ$ ($\gamma = 0$) to $\alpha = 0^\circ$ ($\gamma \to \infty$). From the derivative of the finite strain solution of Eq. (5), the incremental principal strains are related to the applied shear as:

$$d\varepsilon_1 = \frac{d\gamma}{\sqrt{4+\gamma^2}}, \quad d\varepsilon_2 = 0 \quad , \quad d\varepsilon_3 = -d\varepsilon_1 \tag{8a-c}$$

Assuming that the material axes (such as the RD-TD shown in Figure 1) rotate according to the applied deformation (neglecting plastic and microstructural spin), the rotation tensor to locate the material axes is obtained from a polar decomposition of the deformation gradient of Eq. (1) as:

$$R = \frac{1}{\sqrt{4+\gamma^2}} \begin{bmatrix} 2 & \gamma & 0 \\ -\gamma & 2 & 0 \\ 0 & 0 & \sqrt{4+\gamma^2} \end{bmatrix}, \tag{9a}$$

$$x' = Rx \tag{9b}$$

where x and x' are the reference and rotated frames, respectively. Note that the analysis of Chen *et al.* (2018) determined the location of the material axes in torsion using an integral of the vorticity tensor in Eq. (4) to obtain the rotation tensor as

$$\int \boldsymbol{W} = \begin{bmatrix} 0 & \gamma/2 & 0 \\ -\gamma/2 & 0 & 0 \\ 0 & 0 & 0 \end{bmatrix} \to R = \begin{bmatrix} \cos(\gamma/2) & -\sin(\gamma/2) & 0 \\ \sin(\gamma/2) & \cos(\gamma/2) & 0 \\ 0 & 0 & 1 \end{bmatrix} \tag{10}$$

which is an approximation to the exact solution of Eq. (9a).

2.2. Stress State and Equivalent Strain

In a simple shear test, the applied stress tensor in the global coordinate frame is:

$$\sigma = \begin{bmatrix} \sigma_{11} & \sigma_{12} & 0 \\ \sigma_{21} & \sigma_{22} & 0 \\ 0 & 0 & 0 \end{bmatrix} \approx \begin{bmatrix} 0 & F/A_0 & 0 \\ F/A_0 & 0 & 0 \\ 0 & 0 & 0 \end{bmatrix}, \tag{11}$$

$$eig(\sigma) = \begin{bmatrix} \sigma_1 \\ \sigma_2 \\ \sigma_3 \end{bmatrix} = \begin{bmatrix} F/A_0 \\ 0 \\ -F/A_0 \end{bmatrix} \tag{12}$$

in which F is the applied shear force, and A_o is the initial shear gauge area which remains constant during deformation. The magnitude of the normal stress components in Eq. (11) are negligibly small and are further discussed in Section 2.2.1. The local strains in the gauge area of shear specimens are measured using DIC techniques. The incremental plastic work balance of the applied stress and plastic strain is:

$$dw^p = \bar{\sigma} d\varepsilon_{eq}^p = \tau d\gamma^p \tag{13}$$

Assuming no material softening, $\sigma_{eq} = \bar{\sigma}$, the equivalent plastic strain increment is:

$$d\varepsilon_{eq}^p = \left(\frac{\tau}{\sigma_{eq}}\right)_\beta d\gamma^p = \left(\frac{\tau}{\sigma_{eq}}\right)_\beta \left(d\gamma - \frac{\tau}{G}\right) \tag{14}$$

where G is the shear modulus and was assumed to be constant and independent of direction (isotropic elasticity). In Eq. (14), τ/σ_{eq} is the shear-to-equivalent stress ratio at the current orientation of the material axes denoted by the angle β. This angle is governed by the initial orientation of the material axes, β_i (see Figure 1), and the applied shear γ, and can be determined using the rotation tensor of Eq. (9) as:

$$\beta = \beta_i - \varphi \tag{15a}$$

$$\beta = \beta_i - \left[\frac{1}{2}\tan^{-1}\left(\frac{4-\gamma^2}{4\gamma}\right)\right] \tag{15b}$$

Section 2.3 will address the determination of τ/σ_{eq} and the conversion of the shear stress to an equivalent stress.

2.2.1. Normal Stress in Simple Shear

In general, simple shear gives rise to both shear and normal stresses due to the induced rotation leading to:

$$\sigma = \begin{bmatrix} \sigma_{11} & \sigma_{12} & 0 \\ \sigma_{12} & \sigma_{22} & 0 \\ 0 & 0 & 0 \end{bmatrix} = \begin{bmatrix} \sigma_{11} & \sigma_{12} & 0 \\ \sigma_{12} & -\sigma_{11} & 0 \\ 0 & 0 & 0 \end{bmatrix} \tag{16}$$

The condition for the shear stress state to be plane stress, $\sigma_{33} = 0$, and purely deviatoric, $J_3 = \det(\boldsymbol{s}_{ij}) = 0$, enforces the expected result of

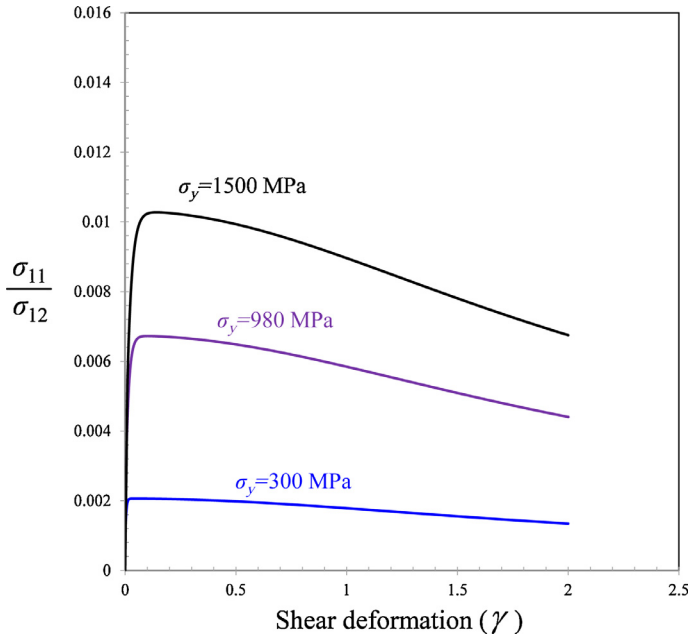

Figure. 2. Development of normal stress in simple shear for an elastic-perfect plastic material with different yield strengths and a shear modulus of steel at 84 GPa. The normal stresses are equal-and-opposite such that $\sigma_{22} = -\sigma_{11}$.

a vanishing hydrostatic stress. The normal and principal stress components are deviatoric and are thus equal and opposite such that $\sigma_{22} = -\sigma_{11}$ and $\sigma_1 = -\sigma_3$. The development of the normal stress has been investigated using isotropic yield functions from a numerical perspective for various cases by Bruhns *et al.* (1999), Rahmaan *et al.* (2017) and Butcher and Abedini (2017). For experimental characterization of anisotropic materials in shear, the development of normal stresses warrants closer investigation.

To provide insight into the evolution of the stress components, we can adapt the procedure of Bruhns *et al.* (1999) to rely upon the measured shear stress instead of assuming a yield function to perform the analysis. Assuming the associated flow rule, the logarithmic objective rate of true stress in simple shear for an elastic-plastic material can be written as:

$$\overset{o}{\sigma} = \dot{\sigma} + \sigma\Omega^{\log} - \Omega^{\log}\sigma = \mathbb{L}: (\boldsymbol{D} - \boldsymbol{D^p}) = 2G\left(\boldsymbol{D} - \left(\frac{\tau}{\sigma_{eq}}\right)d\gamma\boldsymbol{N}\right) \tag{17}$$

where $\boldsymbol{N}$ is the normal tensor and $\Omega^{\log}$ is the logarithmic spin tensor:

$$\Omega^{\log} = \frac{d\gamma}{4}\left(\frac{4}{4+\gamma^2} + \frac{\gamma}{\sqrt{4+\gamma^2}\sinh^{-1}(\gamma/2)}\right)\begin{bmatrix} 0 & 1 & 0 \\ -1 & 0 & 0 \\ 0 & 0 & 0 \end{bmatrix} \tag{18}$$

The normal tensor must now be determined. The applied deformation gradient for shear enforces isochoric and plane strain deformation by definition in Eq. (1) and is independent of whether the material is assumed to be elastic or plastic. For plastic deformation, the imposed strain field forms a constraint upon the normal vectors such that $N_{22} = -N_{11}$ and $N_1 = -N_3$. The principal stress and principal normal vectors are readily obtained from plastic work balance and are:

$$s_1 = \sigma_1 = \sqrt{{\sigma_{11}}^2 + \sigma_{12}^2} = \tau, \tag{19}$$

$$N_1 = \sqrt{{N_{11}}^2 + N_{12}^2} = \frac{1}{2}\frac{\sigma_{eq}}{\sigma_1} = \frac{1}{2}\left(\frac{\sigma_{eq}}{\tau}\right) \tag{20}$$

To avoid selecting a yield surface that may introduce bias, we can define an instantaneous flow rule for shear to relate the two deviatoric stresses with the respective normal vectors through an unknown constant, κ, as$N_{ij} = \kappa(s_{ij}/\sigma_{eq})$ such that:

$$N_{11} = \kappa\frac{\sigma_{11}}{\sigma_{eq}}, \tag{21}$$

$$N_{12} = \kappa\frac{\sigma_{12}}{\sigma_{eq}} \tag{22}$$

Combining Eqs. (19-22), it is straightforward to obtain:

$$\kappa = \frac{\sigma_{eq}}{\sigma_1}N_1 = \frac{1}{2}\left(\frac{\sigma_{eq}}{\tau}\right)^2 \tag{23}$$

Note that anisotropy in Eq. (23) for an assumed yield function can be accounted for by the ratio of $\sigma_{eq}/\tau = \sigma_{eq}/\sigma_1$ in shear loading evaluated with respect to the current material axes. Making use of $\dot{\boldsymbol{\sigma}} = d\gamma\frac{d\sigma}{d\gamma}$, a differential equation for the shear stress is obtained from Eq. (17) as:

$$\frac{d\sigma_{12}}{d\gamma} = G\left(1 - \frac{\sigma_{12}}{\tau}\right) - \frac{\tau}{4}\left(\frac{4}{4+\gamma^2} + \frac{\gamma}{\sqrt{4+\gamma^2}\sinh^{-1}(\gamma/2)}\right)\sqrt{1 - \left(\frac{\sigma_{12}}{\tau}\right)^2} \tag{24}$$

that can be readily integrated using the fourth-order Runge-Kutta method to obtain the shear stress and the normal stress follows from Eq. (19). No assumptions of isotropy or anisotropy have been made to obtain Eq. (24) and its integration provides the stress components in the global or reference frame. To demonstrate the development of normal stresses in simple shear we will adopt a fictional model material that is *elastic-perfectly plastic* with $G = 84$ GPa selected to be representative of steel. We will consider three different shear yield strengths of 173 MPa, 566 MPa, and 866 MPa. For reference, the respective shear yield strengths would correspond to von Mises yield strengths of approximately 300 MPa, 980 MPa, and 1500 MPa. The initial conditions to integrate Eq. (24) starting at the onset of plastic deformation are:

$$\tau_{yield} = \frac{\sigma_{12}^{yield}}{2}\sqrt{4 + \gamma_{yield}^2} = \text{constant} \tag{25}$$

$$\left(\frac{\sigma_{11}}{\sigma_{12}}\right)_{yield} = \frac{\gamma_{yield}}{2}, \tag{26a}$$

$$(\sigma_{12})_{yield} = 2G\frac{\sinh^{-1}(\gamma_{yield}/2)}{\sqrt{1 + \gamma_{yield}^2/4}} \tag{26b}$$

As shown in Figure 2, the development of normal stresses with respect to shear is on the order of 1% for steels with a tensile yield strength of ~1500 MPa that is typical for hot stamped steels. The results can be generalized to aluminum or other alloys using the ratio of the shear yield stress to the shear modulus (τ_y/G) for the three cases considered. The relatively simple integration of Eq. (24) avoids the need for a custom user-defined material model with the logarithmic rate to be implemented into a commercial finite-element code such as LS-DYNA which was done in Butcher and Abedini (2017).

The theoretical analysis of simple shear for elastic-perfectly plastic materials confirms that the normal stress can be considered negligible relative to the applied shear stress, which should also hold for pressure-independent anisotropic materials without tension-compression asymmetry. However, it is worth demonstrating that the calibration of the anisotropic yield function may lead to erroneous predictions for the normal stresses. It is critical to emphasize that although an anisotropic yield function can be used to account for anisotropy of the hardening response from the measured shear stress as done by Chen *et al.* (2018), the integration of the same yield function in simple shear under associated flow does not necessarily produce the same result.

To demonstrate the importance of anisotropic yield function calibration on the development of normal stresses, single-element simulations of simple shear were conducted using the commercial finite-element code, LS-DYNA. The associated Yld2000-2d model of Barlat *et al.* (2003) was employed (see Section 4) for an aluminum alloy AA7075-T6. The coefficients of the Yld2000-2d model for this material were determined by Abedini *et al.* (2018b) using a "conventional calibration" method using tensile stresses and R-values as well as a modified calibration technique that enforced equal and opposite principal strains in shear ($\varepsilon_1 = -\varepsilon_3$). Recently, Butcher and Abedini (2019) provided a general solution for the plastic constraints for pressure-independent plasticity in generalized plane strain conditions of which the so-called shear constraint of Abedini *et al.* (2018b) is included. It was demonstrated by Abedini *et al.* (2018b) that the conventional calibration of Yld2000-2d could introduce a non-physical hydrostatic stress in simple shear but the magnitude of the normal stresses was not reported. It is possible that large normal stresses could develop due to anisotropy but the hydrostatic stress remains zero since they are theoretically equal in magnitude but opposite in sign.

Re-visiting the analysis of Abedini *et al.* (2018b) for AA7075-T6, it is evident from Figure 3 that the conventional calibration of anisotropic yield criteria that is only focused upon tensile stresses and R-values can lead to considerable non-zero normal stresses. When the anisotropic yield function was calibrated to enforce the shear constraint upon the normal vectors required by pressure-independent plasticity and the deformation gradient of Eq. (1), the hydrostatic stress remains close to zero. This result highlights the importance of calibration of associated anisotropic yield criteria in shear stress states. Note that the difference between the shapes of the curves in Figures 2 and 3 is due to the objective rates since the LS-DYNA code utilizes the Jaumann rate while a logarithmic rate was used in the analytical solution shown in Figure 2.

It is emphasized that the solutions in Figures 2 and 3 for the relative magnitude of the normal stresses are derived with respect to the reference frame and not the material frame. The normal stresses in the reference frame can be neglected to simplify the experimental analysis of the shear tests. Only the shear stress in Eq. (16) is significant and will be transformed into the material frame to then account for shear anisotropy. *The normal stresses in the material frame may not be negligible but will remain equal and opposite*.

As a consequence of the negligible normal stress in the reference frame, the principal stress directions remain essentially constant at ± 45° to the applied shear direction. The principal stress and *incremental* principal strains of Eqs. (2) and (11) are always coaxial and aligned so that the stress and strain increments are proportional. However, the principal stress and *total* principal strain (Eq. 5) are not proportional and are only aligned at the onset of yield for a rigid-plastic material. The divergence of the principal stress and principal strain directions is shown in Figure 4 as a function of the applied shear. This should not be confused with the rotation of the *material frame* which is governed by the rotation tensor of Eq. (9).

2.3. Conversion of Shear Stress-Strain to Equivalent Stress-Strain

With the fundamentals of shear of anisotropic materials established, we can now describe how the experimental shear stress-strain results can be converted to equivalent stress-strain data to calculate hardening behaviour or flow curves of materials to large strains. The incremental plastic work was given in Eq. (13) such that the incremental plastic strain increment can be obtained using work-conjugacy in Eq. (14), restated below:

$$d\varepsilon_{eq}^{p} = \left(\frac{\tau}{\sigma_{eq}}\right)_{\beta} d\gamma^{p} \tag{27}$$

In this equation, the value of shear-to-equivalent stress ratio or the so-called shear ratio, τ/σ_{eq}, is the key to obtain the hardening behaviour from the shear test. The τ/σ_{eq} ratio is used for determining the

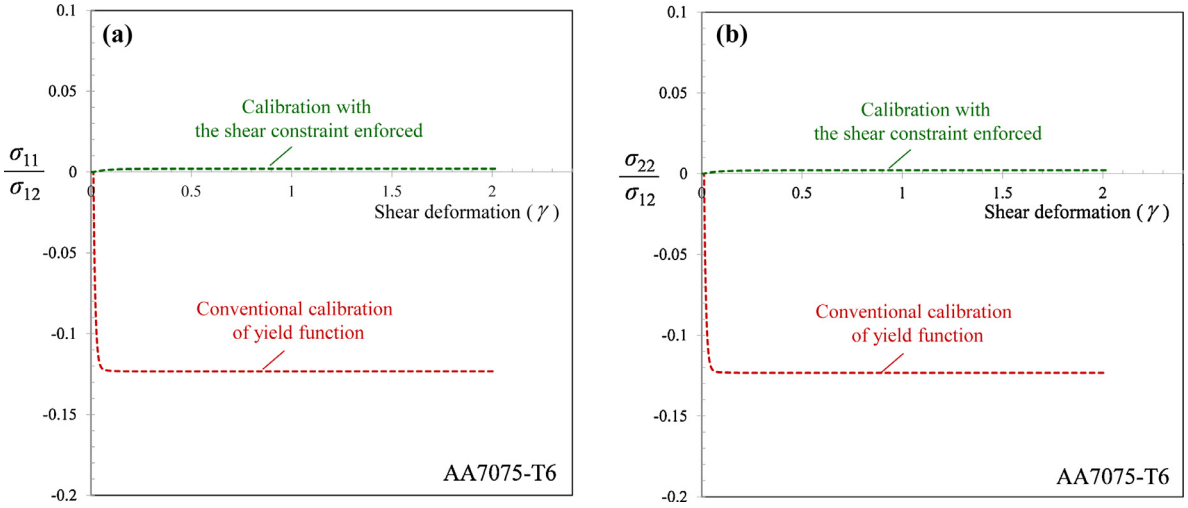

Figure. 3. Development of normal stresses in simple shear for an anisotropic material (AA7075-T6) with and without the shear constraint of Abedini *et al.* (2018b) enforced on an associated Yld2000-2d yield criterion. The solution for the conventional calibration is inconsistent with pressure-independent plasticity since the normal stresses have a similar magnitude with the same sign for the loading case considered.

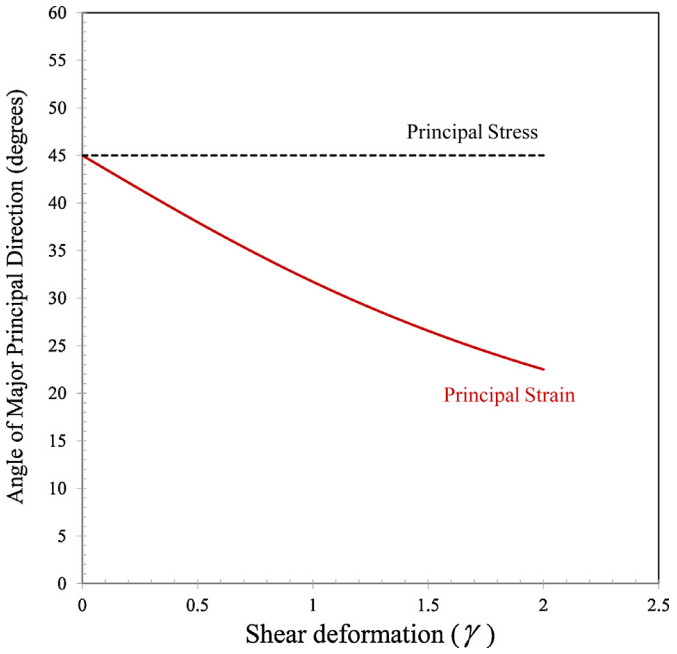

Figure. 4. Comparison of the orientation of the major principal stress and major principal strain obtained using the logarithmic objective rate for an elastic-perfectly plastic material.

equivalent plastic strain (using Eq. 27) and also the equivalent stress by multiplying its inverse to the shear stress:

$$\sigma_{eq} = \left(\frac{\tau}{\sigma_{eq}}\right)_{\beta}^{-1} \tau \tag{28}$$

It is assumed that experimental shear data is available. In the absence of tensile data, τ/σ_{eq} can be estimated by adopting a yield criterion such as the isotropic Hosford yield criterion:

$$\left(\frac{\tau}{\sigma_{eq}}\right)^{Hosford} = \frac{1}{(1 + 2^{(a-1)})^{1/a}} \tag{29}$$

in which "a" is the exponent of the yield criterion and $a = 2$ reduces the model to von Mises with a shear-to-equivalent stress ratio of 0.577. Suggested exponents for isotropic BCC and FCC materials are $a = 6$ and $a = 8$, respectively (Hosford, 1996), with shear-to-equivalent stress ratios of 0.558 and 0.545.

A more robust approach to find τ/σ_{eq} is to perform both a tensile and a shear test as proposed by Rahmaan *et al.* (2017). These two tests are complementary and are conducted to extract the stress-strain history and obtain τ/σ_{eq} at the same level of plastic work. In terms of the test directions, Rahmaan *et al.* (2017) suggested that the tensile and shear tests should be performed such that they have the same major principal direction. Note that the shear state has two equal and opposite principal stresses oriented at ± 45° with respect to the maximum shear direction. For instance, Rahmaan *et al.* (2017) suggested that if a tensile test is performed in the RD, the complementary shear test should be conducted with the shear load along the 45°, corresponding to point ① in Figure 5, with the major principal direction along the RD. Once the shear-to-equivalent stress ratio is obtained, the hardening response of the material can be derived using the procedure described above. In this approach, no yield criterion is required to be assumed since the shear ratio is determined experimentally.

For an orthotropic material that does not exhibit tension-compression asymmetry, several conditions are dictated due to symmetry of the yield surface. For instance, the shear states associated with Points ① and ③ in Figure 5 have the same principal directions but with opposite signs. For a symmetric material, the yield stress is identical at these two points; however, this does not hold for asymmetric materials such as magnesium alloys with HCP crystal structure (Abedini *et al.*, 2017b). Furthermore, for an orthotropic material, the shear yield stresses shown in Figure 5(b) from 0° to 90° will be identical to shear stresses from 90° to 180°. These conditions are in accordance with the orthotropic-symmetric formulation of the Yld2000-2d yield criterion (Barlat *et al.*, 2003) as presented in Section 4.

2.4. Incorporation of Material Frame Rotation and Shear Anisotropy into the Shear Conversion Methodology

The macroscopic plastic work balance that enables the shear conversion in Eq. (27) also holds for anisotropic materials. The shear-to-equivalent stress ratio now becomes a function of the current location of the material axes that evolves with deformation. The rotation of the material axes (RD-TD) with the applied deformation according to Eq. (9) is a first-order approximation that neglects rotation due to plastic and microstructural spin. The methodology of Rahmaan *et al.* (2017) can be directly extended by performing multiple shear tests to obtain τ/σ_{eq} in different directions and interpolating between the discrete values of τ/σ_{eq}. In this approach, the equivalent stress used in the normalization of the shear stress is that of the reference direction (rolling direction, for instance). Using the rotation tensor in Eq. (9), the location of the material axes is derived and the τ/σ_{eq} ratio for that specific orientation of the material axes has to be acquired from a curve similar to Figure 5(b) that specifies shear anisotropy or shear yield strength in different directions. This curve can be obtained experimentally with several shear test orientations. In addition, a yield criterion can be calibrated to the experimental data to predict the shear yield stresses at intermediate angles. Subsequently, the equivalent plastic strain increment is directly determined from the shear test data as:

$$d\varepsilon_{eq}^{p} = \frac{\tau d\gamma^{p}}{\bar{\sigma}} = \left(\frac{\tau}{\sigma_{eq}}\right)_{\beta} d\gamma^{p} = 2\left(\frac{\tau}{\sigma_{eq}}\right)_{\beta} \sqrt{1 + \sinh^2 \varepsilon_1}\, d\varepsilon_1 \left(1 - \frac{\tau}{2G}\right) \tag{30}$$

and the corresponding equivalent stress is readily calculated using the measured shear stress and the current shear stress ratio in Eq. (28). It should be mentioned that Rahmaan *et al.* (2017) assumed that τ/σ_{eq} in Eq. (30) remains constant throughout deformation. It will be shown later that this assumption is reasonable for mildly anisotropic materials. Although the initial material axes directions were considered by Rahmaan *et al.* (2017), the rotation of the material axes with deformation was not taken into account.

The subsequent sections will characterize the experimental shear stress anisotropy of four different automotive alloys and evaluate its influence upon the hardening response. It is important to emphasize that from a theoretical perspective, any interpolation-based strategy is admissible to estimate the shear stress between different test orientations to determine the plastic strain increment in Eq. (30). The accuracy of the interpolation depends upon the shear anisotropy and the number of shear tests performed at intermediate orientations. The methodology of the present study will focus upon using a non-quadratic Yld2000-2d yield function calibrated with multiple shear tests to accurately capture the shear anisotropy which is equivalent to a non-linear interpolation. An alternative interpolation methodology based upon assuming a simple functional form using only the experimental shear stress ratios will also be considered in Section 5.4.

Finally, it is emphasized that the present shear conversion methodology to determine the hardening response inherently assumes *isotropic hardening* behaviour and should not be confused with the assumption of isotropic plasticity. In other words, Bauschinger effects, kinematic hardening, and distortional hardening (Chaboche, 2008; Barlat *et al.*, 2011) are not considered. Distortional hardening could be readily considered for materials with evolving plasticity by extending the interpolation of the shear stress ratio as a function of plastic work. Future work on the methodology should investigate alloys with such

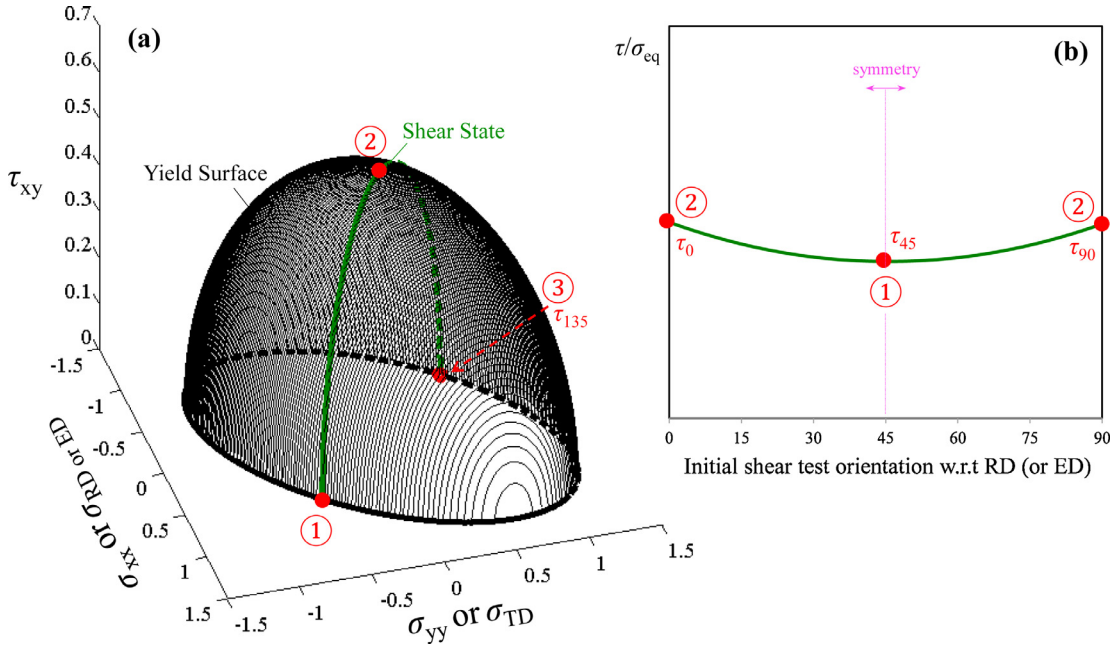

Figure. 5. Schematic views of (a) top half of a yield surface plotted in 3-D in which the shear region is shown in green, and (b) variation of shear yield stress with direction for an orthotropic material.

complex hardening mechanisms along with cyclic loading to activate these mechanisms.

3. Materials and Experimental Data

Four different types of automotive alloys were considered in this work: two advanced high strength dual-phase steel sheets, DP980 and DP1180, with nominal thicknesses of 1.20 mm and 1.00 mm, respectively, as well as 1.55 mm thick AA5182-O aluminum rolled sheet and 2.00 mm thick AA6063-T6 aluminum extrusion from the same lot of extrusions studied by Kohar *et al.* (2016). The uniaxial tensile responses of the materials in different orientations with respect to the rolling or extrusion directions (reference directions) were obtained using standard tensile geometries with the normalized yield stresses and R-values reported in Table 1. Furthermore, shear tests were conducted using a shear specimen geometry adopted from Peirs *et al.* (2012) as shown in Figure 6. The shear tests were performed by a standard tensile frame with the samples fabricated from the materials in multiple orientations with respect to their reference directions to reveal the directional dependency of the shear response. This shear geometry has been analyzed in detail with the aid of finite-element simulations by Peirs *et al.* (2012) and Rahmaan *et al.* (2020) where it is shown that the shear stress that an element at the center of the gauge area experiences can be simply determined from F/A_o in which F is the applied global force and A_o is a constant gauge area. The gauge area is calculated from multiplication of the materials thickness by the gauge length (3.0 mm as shown in Figure 6).

Table. 1
Normalized yield stresses in tension (σ) and shear (τ) with respect to uniaxial tensile stress in the rolling or extrusion directions, and R-values (r) in different directions. The variable w^p corresponds to the plastic work per unit volume. The values in brackets show the standard deviations.

Material	DP1180	DP980	AA5182-O	AA6063-T6
w^p [MJ/m^3]	61.11	70.00	51.50	19.60
σ_0/σ_0	1.000 (0.006)	1.000 (0.000)	1.000 (0.01)	1.000 (0.005)
σ_{15}/σ_0	0.995 (0.003)	1.012 (0.007)	0.972 (0.003)	0.969 (0.007)
σ_{30}/σ_0	0.996 (0.003)	0.995 (0.003)	0.960 (0.002)	0.992 (0.005)
σ_{45}/σ_0	1.004 (0.007)	0.988 (0.005)	0.948 (0.005)	0.975 (0.003)
σ_{60}/σ_0	1.008 (0.008)	1.009 (0.004)	0.935 (0.010)	0.910 (0.003)
σ_{75}/σ_0	1.013 (0.003)	1.018 (0.004)	0.945 (0.004)	1.007 (0.002)
σ_{90}/σ_0	1.025 (0.007)	1.018 (0.003)	0.964 (0.000)	0.996 (0.005)
τ_0/σ_0	0.600 (0.005)	0.591 (0.010)	0.540 (0.010)	0.599 (0.005)
$\tau_{22.5}/\sigma_0$	0.600 (0.008)	0.581 (0.008)	0.517 (0.009)	0.560 (0.002)
τ_{45}/σ_0	0.612 (0.005)	0.608 (0.005)	0.540 (0.007)	0.523 (0.006)
r_0	0.82 (0.01)	0.78 (0.02)	0.60 (0.04)	0.53 (0.05)
r_{15}	0.84 (0.01)	0.79 (0.02)	0.67 (0.02)	0.56 (0.12)
r_{30}	0.90 (0.01)	0.86 (0.03)	0.80 (0.01)	0.38 (0.04)
r_{45}	0.95 (0.01)	1.03 (0.01)	0.91 (0.02)	0.53 (0.03)
r_{60}	0.98 (0.01)	0.96 (0.01)	0.83 (0.01)	0.61 (0.03)
r_{75}	1.00 (0.00)	0.87 (0.03)	0.71 (0.01)	0.77 (0.03)
r_{90}	0.98 (0.01)	0.95 (0.01)	0.70 (0.01)	1.20 (0.39)
r_b	0.94 (0.03)	0.84 (0.06)	1.03 (0.03)	0.36 (0.13)

For all the experiments, full-field DIC techniques were utilized for strain measurements with a virtual strain gauge length of 0.50 mm. Details on DIC analysis using the same shear geometry are provided by Rahmaan *et al.* (2017). The measured DIC strain path of a representative shear test on DP1180 is shown in Figure 6. It can be seen that equal and opposite principal strains are achieved in the experiment as expected for the shear state in the absence of Swift effects (Swift, 1947). Note that tensile and shear data for the same DP980 material was also reported in Noder and Butcher (2019) for a limited number of directions.

The biaxial r-value, r_b, of the materials were characterized by means of the through-thickness compression test on a single-layer disc (Barlat *et al.*, 2003; Tian *et al.*, 2016) with a diameter of 5.0 mm using a custom-made compression rig (Ghaffari *et al.*, 2014). This test consists of successive applications of compressive force followed by careful measurements of the diameters of the disc along the RD and TD under an optical microscope to measure the strains. After each load increment, surfaces of the compression rig in contact with the sample were polished and a thin layer of Teflon® spray was applied to reduce friction. Subsequently, a line was fit to the experimental strain data to estimate the biaxial r-value.

Table 1 summarizes all the experimental characterization data. Note that the stress values given in Table 1 were extracted at the plastic work level corresponding to the onset of diffuse necking in the tensile test direction with the lowest necking strain (limiting direction). It is worth mentioning that all the experiments performed in this study were done with a quasi-static von Mises strain rate of 0.001 s^{-1} and at least four

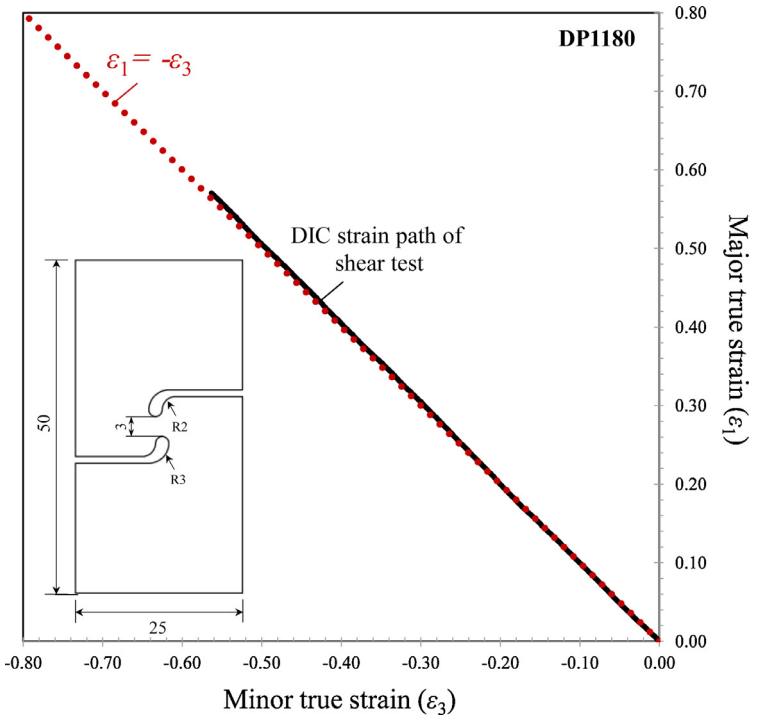

Figure. 6. Shear specimen geometry of Peirs *et al.* (2012) (all dimensions are in millimetres), and measured strain path of a representative shear test on DP1180.

test repeats were conducted to ensure repeatability.

4. Yield Criterion

The yield strength data reported above was used to calibrate the plane stress Yld2000-2d anisotropic yield criterion (Barlat *et al.*, 2003) with the equivalent stress of:

$$\sigma_{eq}^{Yld2000} = \left(\frac{|X'_1 - X'_2|^a + |2X''_2 + X''_1|^a + |2X''_1 + X''_2|^a}{2} \right)^{1/a} \tag{31}$$

in which X_i' and X_i'' are the principal values of the linearly transformed stress tensors, $\boldsymbol{X}'$ and $\boldsymbol{X}''$, that are given by:

$$\boldsymbol{X}' = \mathbf{L}' : \boldsymbol{\sigma}, \tag{32}$$

$$\boldsymbol{X}'' = \mathbf{L}'' : \boldsymbol{\sigma} \tag{33}$$

The eight calibration parameters, $\alpha_{1\text{-}8}$, are embedded in the fourth-order linear stress transformation tensors $\mathbf{L}'$ and $\mathbf{L}''$ for plane stress loading as:

$$\begin{bmatrix} L'_{11} \\ L'_{12} \\ L'_{21} \\ L'_{22} \\ L'_{66} \end{bmatrix} = \begin{bmatrix} 2/3 & 0 & 0 \\ -1/3 & 0 & 0 \\ 0 & -1/3 & 0 \\ 0 & 2/3 & 0 \\ 0 & 0 & 1 \end{bmatrix} \begin{bmatrix} \alpha_1 \\ \alpha_2 \\ \alpha_7 \end{bmatrix}, \tag{34}$$

$$\begin{bmatrix} L''_{11} \\ L''_{12} \\ L''_{21} \\ L''_{22} \\ L''_{66} \end{bmatrix} = \frac{1}{9} \begin{bmatrix} -2 & 2 & 8 & -2 & 0 \\ 1 & -4 & -4 & 4 & 0 \\ 4 & -4 & -4 & 1 & 0 \\ -2 & 8 & 2 & -2 & 0 \\ 0 & 0 & 0 & 0 & 9 \end{bmatrix} \begin{bmatrix} \alpha_3 \\ \alpha_4 \\ \alpha_5 \\ \alpha_6 \\ \alpha_8 \end{bmatrix} \tag{35}$$

In the present paper, a least-square minimization approach was utilized to determine $\alpha_{1\text{-}8}$ from the experimental data given in Table 1. The exponent of the yield function "a" in Eq. (31) was set to 6 for BCC (DP1180 and DP980) and 8 for FCC (AA5182-O and AA6063-T6) alloys as suggested by Hosford (1996). Note that in order to calibrate the model, a non-associated flow rule was employed in which the coefficients of the Yld2000-2d model were calibrated to the experimental data of yield stresses to derive stress-potentials or yield loci of the materials. Similarly, an independent set of coefficients could be calibrated to describe the direction of plastic flow through plastic potentials within the non-associated framework but is not required for performing the shear conversion to obtain the hardening response. The conversion method can also be effectively applied under associated flow rule provided that the yield function (that is identical to the plastic potential by definition) is properly calibrated to be in accordance with the mechanics of generalized plane strain deformation that includes shear state as well. Under such deformation modes, one principal strain remains zero and should be enforced upon calibration of the model (Butcher and Abedini, 2019).

5. Results and Comparison

5.1. Calibrated Yield Loci for Shear Interpolation

The coefficients of the Yld2000-2d criterion calibrated using experimental data of the four materials are given in Table 2. The

Table. 2
Coefficients of the Yld2000-2d yield function for shear interpolation. The calibration was performed with an emphasis upon obtaining best agreement with the shear stress which is required to obtain the hardening response from the shear test data. The R-values were not used in the calibration of the yield function.

Coefficient	DP1180	DP980	AA5182-O	AA6063-T6
α_1	0.9236	1.8511	0.7831	1.0239
α_2	0.9231	-0.4055	1.2461	1.0896
α_3	1.0018	-1.4455	-1.2697	1.4699
α_4	1.0152	-1.0251	-1.0389	1.0598
α_5	1.0180	-0.2643	1.0327	-0.9579
α_6	0.9036	1.3100	0.9998	-0.9274
α_7	0.9030	0.6386	-0.9403	0.6865
α_8	-1.1278	1.6218	-1.7023	-1.6899
a	6.00	6.00	8.00	8.00

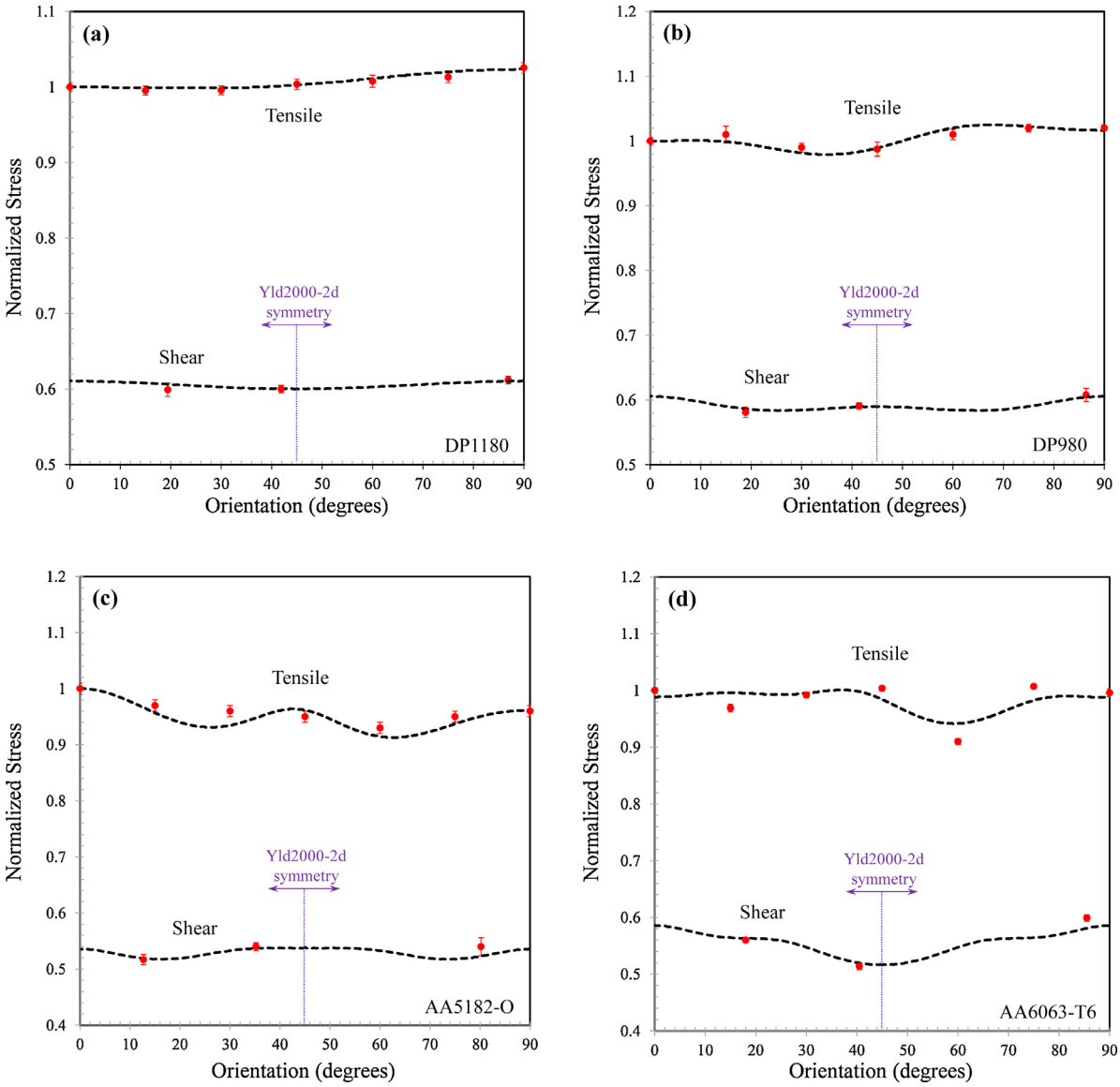

Figure. 7. Normalized stress in different orientations with respect to the reference direction for (a) DP1180, (b) DP980, (c) AA5182-O, and (d) AA6063-T6. Red symbols show the experimental data. The calibration was performed with an emphasis upon obtaining best agreement with the shear stress which is required to obtain the hardening response from the shear test data. For orthotropic-symmetric materials, normalized shear stress is symmetric about the 45° orientation.

predictions of the model in terms of variations of normalized tensile and shear yield stresses in different orientations with respect to the reference (rolling or extrusion) directions for DP1180, DP980, AA5182-O, and AA6063-T6 are shown in Figures 7(a-d), respectively. For comparison, the experimental data measured in the present study are also depicted in Figure 7 with red symbols. Overall, it can be seen that the Yld2000-2d model is able to capture the anisotropic yield strengths in tension and shear to relatively good accuracy. These good correlations include directional dependency of shear stresses which is of high importance for measuring flow curves of the materials from shear test results using the proposed technique described in Section 2.

Note that the shear stress ratios of the four materials were measured at the plastic work levels listed in Table 1 that corresponds to the plastic deformation level at which tensile test with the lowest necking strain reached the onset of necking. To reach this plastic work level, there are some material frame rotations in the shear tests with the magnitudes that depend on the materials (~3.6° for DP980, ~3.1° for DP1180, ~4.5° for AA6063-T6 and ~9.8° for AA5182-O). Therefore, the shear angles are slightly different than the initial specimen fabrication angles and are reflected in the experimental data reported in Figure 7.

5.2. Hardening Response

Using the procedures described in Sections 2.3 and 2.4, the hardening response of the materials were obtained from the shear data. Two approaches were considered:

Method 1 - Shear Isotropy: This approach is in accordance with Rahmaan *et al.* (2017) where the shear ratio, τ/σ_{eq}, for a given direction of interest is held constant over the range of plastic work used in the shear conversion. The results of shear tests in the 45° orientation were used (principal directions along the RD/ED and TD or Point ① in Figure 5), and the shear stress-strain results were converted to equivalent stress-strain data assuming a constant shear-to-equivalent stress ratio ($\tau/\sigma_{eq} = \tau_{45}/\sigma_{eq}$).

Method 2 – Shear Anisotropy: Shear anisotropy is considered by accounting for variations of τ/σ_{eq} during deformation due to the material axes rotation. Similar to the previous approach, the results of the shear test in the 45° orientation were used. However, the shear stress-strain results were converted to equivalent stress-strain data by incorporation of material frame rotation by utilizing non-constant τ/σ_{eq} values determined from the yield criterion calibrated by means of the

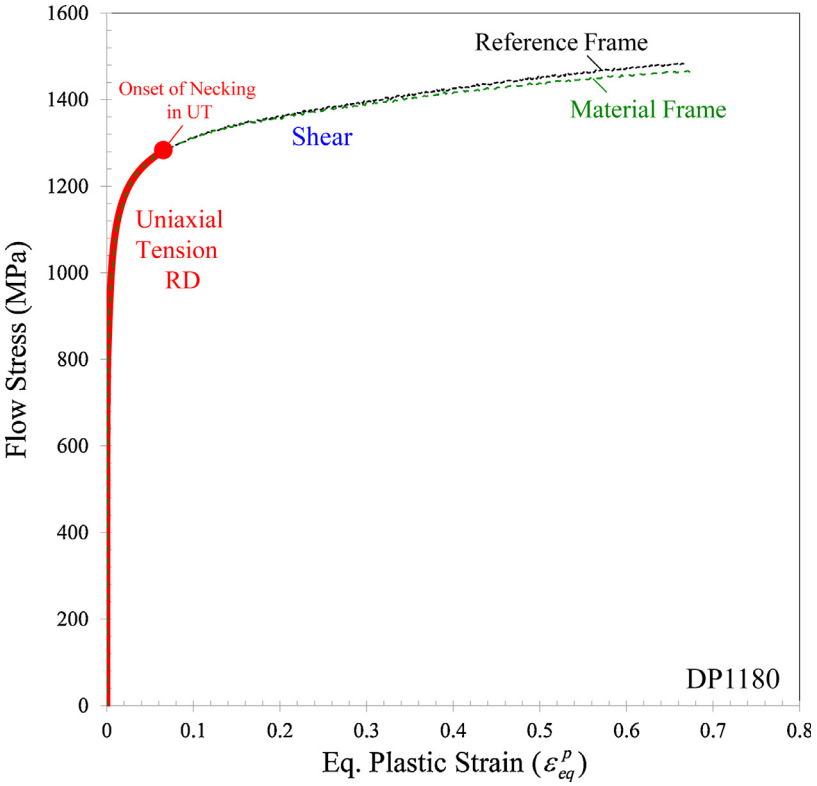

Figure. 8. Hardening response of DP1180 obtained using uniaxial tension and simple shear tests in the rolling direction. The "Reference Frame" corresponds to a constant value for τ/σ_{eq}. The "Material Frame" is associated with accounting for rotation of the material axes and the interpolation τ/σ_{eq} using the calibrated Yld2000-2d yield function. The uniaxial tensile data (shown in red) is limited to low strains by the onset of diffuse necking.

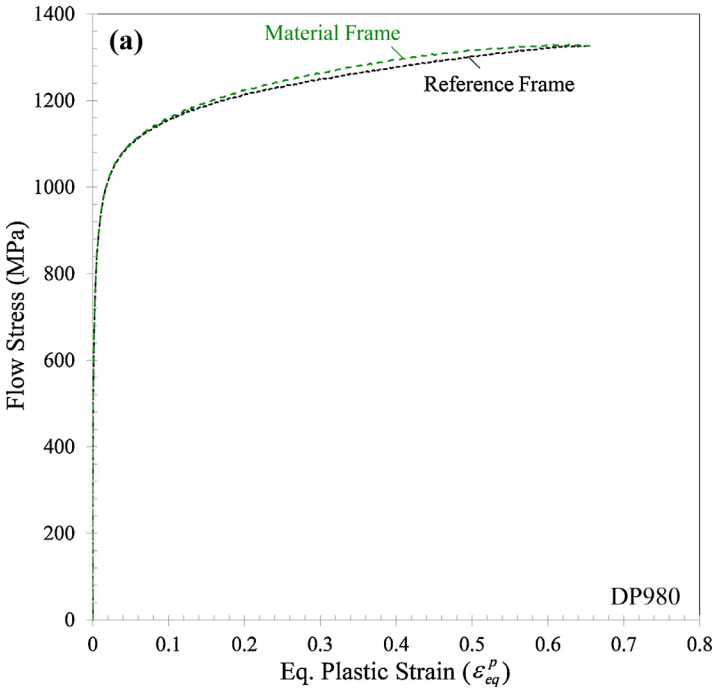

Figure. 9. Hardening responses of (a) DP980, (b) AA5182-O, and (c) AA6063-T6 obtained using shear tests in the rolling and extrusion directions, respectively. The "Reference Frame" corresponds to a constant value for τ/σ_{eq}. The "Material Frame" is associated with accounting for rotation of the material axes and the interpolation of τ/σ_{eq} using the calibrated Yld2000-2d yield function.

experimental data including shear tests in multiple orientations as shown in Figure 7.

Using the two approaches above, the hardening response of DP1180 sheet was obtained as depicted in Figure 8. For comparison, the result of a uniaxial tensile test in the RD is also shown in Figure 8. It is apparent that the tensile data is limited by the onset of localization at a low strain of ~0.06 while the shear test increases the available range of strain by an order of magnitude to over 60%.

In terms of the two methodologies used to convert the shear data, the stress-strain curve derived by assuming a constant τ/σ_{eq} (labelled as reference frame in Figure 8) at small strains is in excellent agreement with the curve determined by accounting for material axes rotation (non-constant τ/σ_{eq}) labelled as material frame in Figure 8. This behaviour is expected since there is no significant rotation of the material

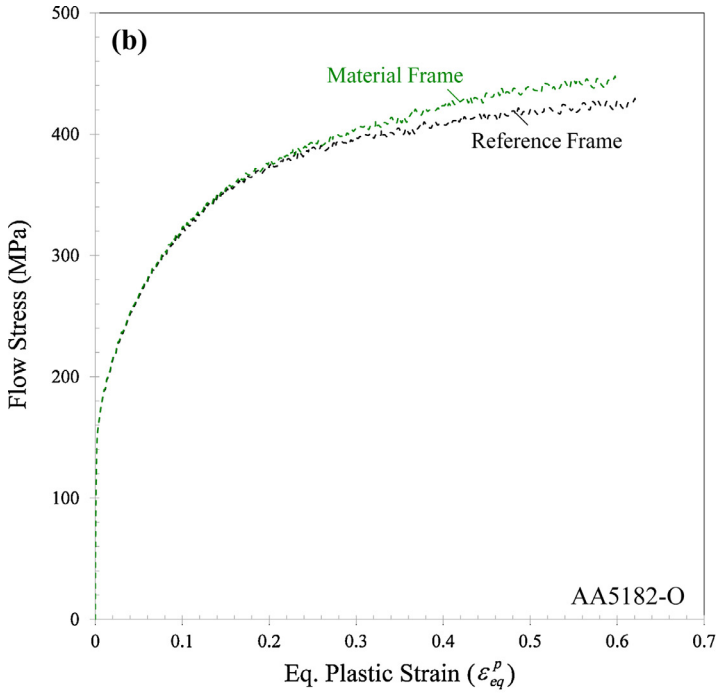

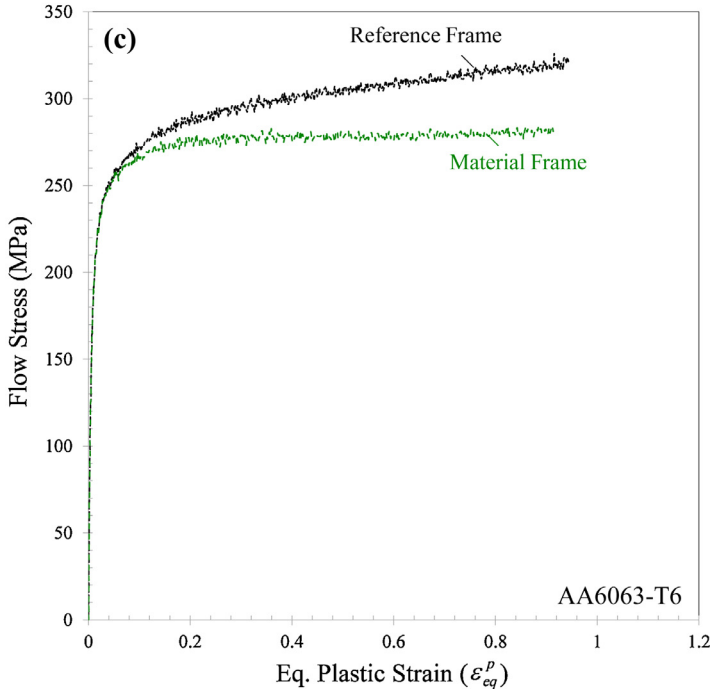

Figure. 9. (*continued*)

Table. 3
Coefficients of the modified Hockett-Sherby model calibrated using the tensile and shear data.

Coefficient	$\bar{A}$	$\bar{B}$	$\bar{C}$	$\bar{D}$	$\bar{E}$
DP980 sheet	501.93	1092.85	10.17	0.50	310.13
DP1180 sheet	665.41	1233.64	15.31	0.58	286.85
AA5182-O sheet	140.46	284.73	18.83	1.05	213.72
AA6063-T6 extrusion	91.21	271.79	19.94	0.74	9.40

frame at small strains. For larger strains, the equivalent stress considered the rotation of the material frame is approximately 1.5% higher. This difference is due to the consecutive rotation of the material frame leading to activation of different shear orientations and consequently a non-constant τ/σ_{eq} ratio caused by shear anisotropy that was revealed by the experiments (shown in Figure 7a). However, since DP1180 is relatively isotropic, this small level of difference can be considered negligible and possibly within the experimental variation. Thus, the shear conversion technique of Rahmaan *et al.* (2017) using a constant shear-to-equivalent stress ratio appears to be sufficient for this DP1180 steel.

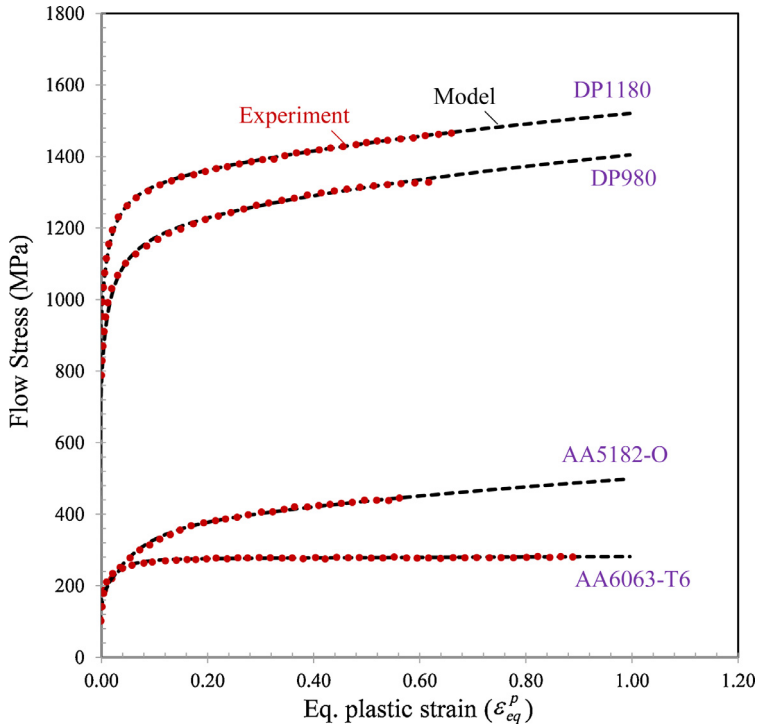

Figure. 10. Comparisons of the calibrated MHS hardening model with the experimental stress response obtained using tensile and shear tests in the rolling or extrusion direction.

Table. 4
Coefficients of the interpolation function of Eq. (37) to describe shear anisotropy of AA5182-O and AA6063-T6.

Coefficient	$\bar{a}$	$\bar{b}$	$\bar{c}$	$\bar{d}$
AA5182-O sheet	0.0115	8.0	0.5891	0.5285
AA6063-T6 extrusion	-0.0384	4.0	0.3927	0.5607

Figures 9(a)-(c) illustrate the hardening behaviour in the reference (rolling or extrusion) direction of DP980, AA5182-O, and AA6063-T6, respectively. Similar to DP1180, the DP980 exhibits up to 2% difference between the flow curves measured using the two techniques. Nevertheless, AA5182-O shows an approximately 5% higher response when the stress-strain curve of the material is determined by considering the material frame rotation. The most remarkable difference between the hardening curves is exhibited in the hardening curves of AA6063-T6 extrusion (15% difference). This behaviour is in accordance with a higher degree of anisotropy in the aluminum alloy. In particular, the AA6063-T6 extrusion has dominant textural components due to its manufacturing process. The higher directional sensitivity in the shear response of the aluminum alloys, as seen in Figures 7(c) and (d), leads to more pronounced contrasts in the hardening curves when an instantaneous τ/σ_{eq} is used. Note the oscillations in the stress response of AA5182-O in Figure 9(b) is due to the Portevin-Le Châtelier (PLC) effects that are known to exist for Mg-Al alloys.

5.3. Constitutive Fits

To describe the isotropic hardening response of the materials obtained to large strain levels using the shear tests, the flexible modified Hockett-Sherby (MHS) model was selected

$$\sigma_{eq} = \bar{B} - (\bar{B} - \bar{A})[\exp(-\bar{C}(\varepsilon_{eq}^{p})^{\bar{D}})] + \bar{E}\sqrt{\varepsilon_{eq}^{p}} \tag{36}$$

where $\bar{A}$, $\bar{B}$, $\bar{C}$, $\bar{D}$, and $\bar{E}$ are the calibration coefficients. The MHS model was calibrated using least squares minimization using Matlab® and the coefficients are tabulated in Table 3 for each alloy. A comparison of the MHS model with the experimental stress response for each material is shown in Figure 10 with good agreement obtained over the range of strain considered.

5.4. Evaluation of an Alternative Interpolation Method for Shear Anisotropy

In the present study the shear states in different orientations were experimentally characterized while an anisotropic yield criterion (Yld2000-2d) was adopted to provide a continuous interpolation of the shear yield stress between calibration points where experimental data was not available. However, assuming a yield surface is not a requirement, provided that a large number of experimental shear data in different directions is available such that a mathematical relation can be fit to the experimental data with high confidence. The shear conversion technique in Eq. (30) only needs the uniaxial tension in the reference direction to be characterized with the shear anisotropy so that a relation for τ/σ_{eq} with orientation can be established. Once this relationship is derived, the technique can be effectively applied without prior knowledge of the yield surface.

To demonstrate the alternative interpolation strategy, a simple trigonometric function in the form of Eq. (37) can be used to interpolate the shear-to-equivalent stress ratio:

$$\frac{\tau}{\sigma_{eq}} = \bar{a}\sin[\bar{c}(\theta - \bar{d})] + \bar{b} \tag{37}$$

The two aluminum alloys were selected to calibrate Eq. (37) because they had the largest shear anisotropy relative to the DP steels. The coefficients of Eq. (37) were calibrated to the experimental shear data, and their values are presented in Table 4.

Figure 11 compares the predicted distributions for shear stress using Yld2000-2d and Eq. (37). The resulting hardening responses for the two methods for AA5182-O and AA6063-T6 are shown in Figure 12. It can be seen that both models are in good agreement, as shown in Figure 12, although there are some mild deviations. The advantage of assuming a

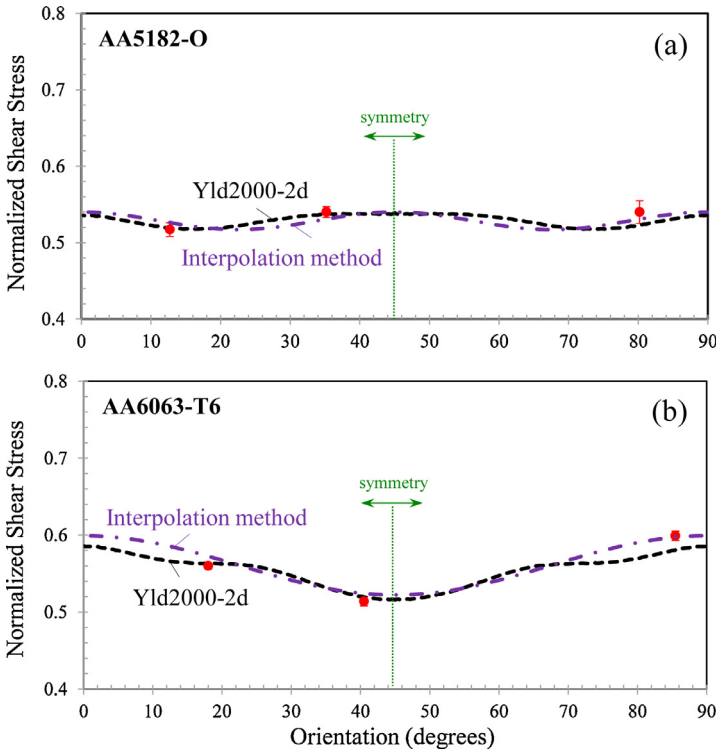

Figure. 11. Normalized shear stress in different orientations with respect to the rolling direction for (a) AA5182-O and (b) the extrusion direction for AA6063-T6. Red symbols show the experimental data.

simple interpolation function such as Eq. (37) is that only the shear test data and the tensile stress in the reference direction are required and the conversion process is simplified even for severely anisotropic materials such as the extrusion. However, from an academic perspective, it may be preferable to calibrate an anisotropic yield function such as the Yld2000-2d that includes the available tensile data to perform a non-linear interpolation under restrictions of convexity that control the shape of the yield surface.

6. Discussion

6.1. Main Factors Influencing the Shear Conversion Technique

It can be inferred that there are two primary factors that influence the hardening response of materials obtained from shear tests:

1. **Degree of anisotropy**: For relatively isotropic materials, such as the two dual-phase sheets of steel, DP980 and DP1180 studied in the present study, using a constant τ/σ_{eq} to convert the shear data is sufficient and the shear conversion technique of Rahmaan *et al.* (2017) appears valid. For AA5182-O, using a constant shear-to-equivalent stress ratio provides a reasonable approximation to a moderate strain level of about 0.2 but should account for shear anisotropy at larger strains or else it would underestimate the hardening response. The AA6063-T6 requires that shear anisotropy be considered in the analysis; otherwise, the hardening rate would have been significantly overestimated.

2. **Shear Ductility**: The extent of material frame rotation in simple shear is a function of the applied deformation (see Eq. 9). In other words, the importance of accounting for frame rotation depends upon the shear failure strain. For a severely anisotropic material with low shear ductility, such as ZEK100 magnesium alloys (Abedini *et al.*, 2017a), accounting for material frame rotation may not make a notable difference because the strains are not large enough to cause an appreciable rotation of the material frame prior to fracture. Note that none of the materials investigated in this work fall in the low-ductility category since they all have equivalent plastic strains at fracture in excess of 0.60 corresponding to at least ~28° rotation.

6.2. Implications on Choice of Shear Test Geometry

The methodology presented in this study assumes the selection of an appropriate shear test geometry such that homogeneous strain and stress fields are achieved in the gauge region throughout deformation. Inappropriate shear test geometries may cause a divergence from simple shear loading with deformation and can be better investigated with the aid of finite-element simulations. The goal of the present paper was to establish a method for extracting hardening response of anisotropic materials assuming that experimental data in simple shear is available.

Premature edge fracture can be an issue in simple shear tests that limits the strain level used to obtain the hardening response. Alternatively, the onset of shear localization prior to fracture may occur which coincides with the formation of a secondary shear band of intense local strain that cannot be captured by conventional DIC strain measurement. As described by Rahmaan *et al.* (2017), the Zener-Holloman criterion (Zener and Hollomon, 1944) that is based upon the peak-load in shear can be used to assist in determining a cut-off strain for usable shear data. The onset of the peak load in a shear test can be caused by material softening (damage), localization into a secondary shear band and/or the onset of edge cracking of the shear specimen. Alternatively, in-plane torsion tests can be utilized for isotropic sheet metals which have been reported to provide high strains to fracture (Yin *et al.*, 2012).

6.3. Notes on Response of AA6063-T6 Extrusion

Among the four materials studied in this work, AA6063-T6 extrusion displayed the most severe anisotropic behaviour in shear. Figure 13 presents an electron-backscatter diffraction (EBSD) map and the corresponding pole figure of the through-thickness microstructure

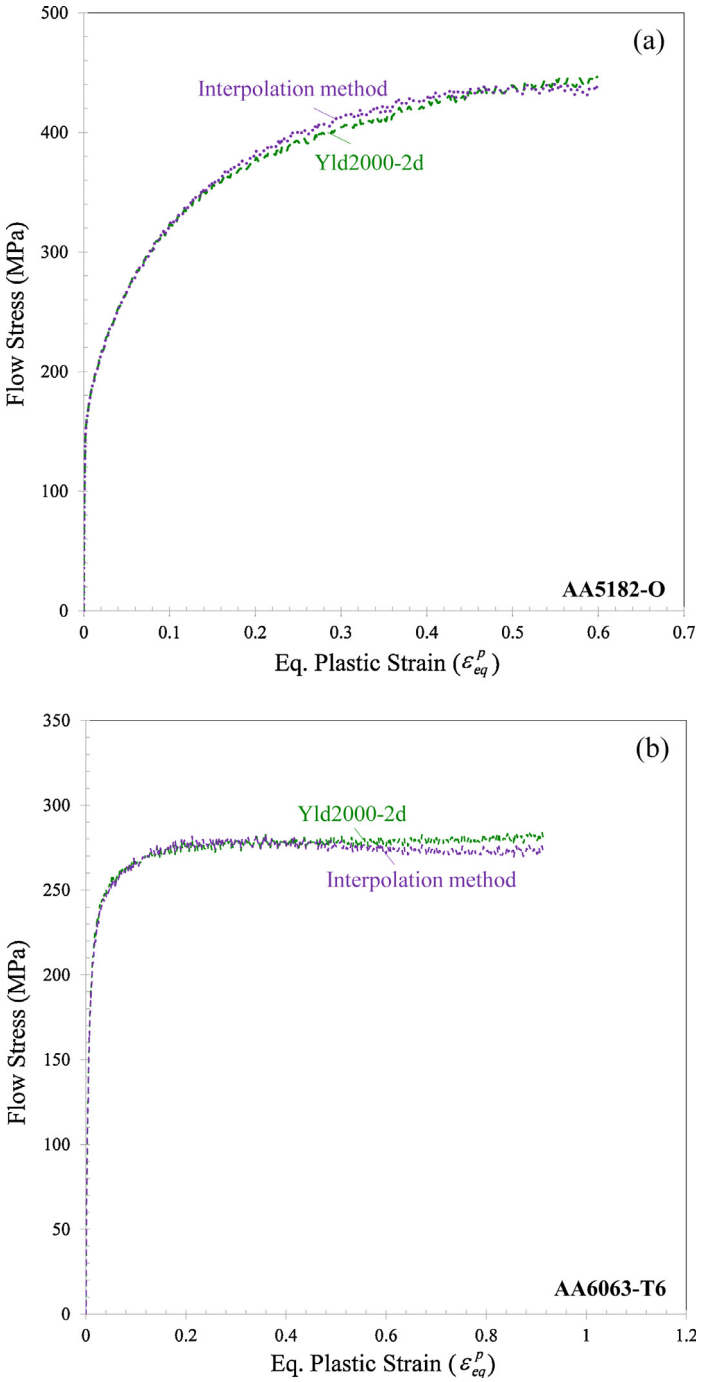

Figure. 12. Comparison of the hardening response of (a) AA5182-O and (b) AA6063-T6 using an interpolation for shear anisotropy using Yld2000-2d and the phenomenological form of Eq. (37) referred to as 'Interpolation method'.

for the AA6063-T6 aluminum extrusion. This severe anisotropy arises from the complex deformation paths and high temperatures generated in the material during manufacturing that results in a strong heterogeneous microstructure. The core section of the extrusion contains a microstructure that is predominantly cube texture. The outer surfaces of the extrusion (approximately 0.40 mm in thickness on each surface) contain coarse grains that have recrystallized with a predominantly rotated copper texture; this phenomenon is known as the peripheral coarse grain (PCG) structure. The cube dominated core section has four-fold symmetry that lends itself to well-defined orthotropic axes with symmetry. However, the rotated copper texture in the PCG layer has two-fold symmetry where these symmetry axes do not align with the core section. As a result, the aggregated microstructure of the extruded AA6063-T6 results in a loss of unique orthotropic axes that are aligned in the extrusion direction. This loss in orthotropic symmetry is further compounded by the evolution of texture towards preferential directions that is dependent on the deformation state (Kohar *et al.*, 2019a).

To investigate the potential loss of symmetry in the extrusion, supplemental shear testing was performed in additional directions of -22.5°, -45°, and 90° in accordance with the methodology outlined in Section 3 for the AA6063-T6 extruded aluminum alloy. Table 5 summarizes the supplementary experimental data that was performed for the AA6063-T6 alloy. The experimental measurements show that there is no symmetry about ± 45° or ± 22.5°. Furthermore, there is no symmetry between 0° and 90° for this AA6063-T6 extrusion.

As discussed in Section 2, the Yld2000-2d model has been

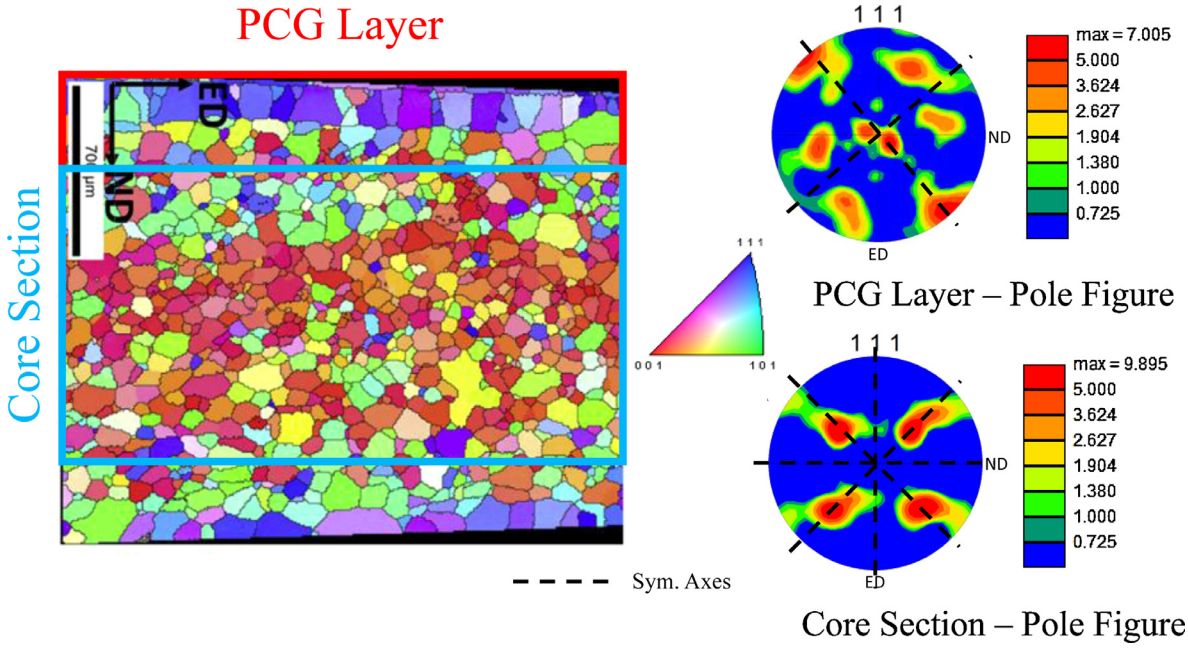

Figure. 13. Through-thickness microstructure of AA6063-T6 material (adapted from Muhammad *et al.*, 2019).

Table. 5
Additional measurements of normalized shear with respect to uniaxial tensile stress in extrusion direction for AA6063-T6 extruded aluminum alloy. The values in brackets show the standard deviations.

τ_0/σ_0	$\tau_{22.5}/\sigma_0$	τ_{45}/σ_0	τ_{90}/σ_0	$\tau_{-22.5}/\sigma_0$	τ_{-45}/σ_0
0.599 (0.005)	0.560 (0.002)	0.523 (0.006)	0.573 (0.002)	0.582 (0.005)	0.548 (0.003)

formulated for orthotropic-symmetric materials and therefore is unable to resolve the response of AA6063-T6 extrusion as illustrated in Figure 14. This result highlights that an enhanced constitutive model, such as a new phenomenological yield function or the physics-based crystal plasticity model (Inal *et al.*, 2010; Dumoulin *et al.*, 2012; Kohar *et al.*, 2019b) may be required to capture the non-orthotropic behaviour observed during simple shear for the AA6063-T6 extruded aluminum alloy.

6.4. Evolution of Anisotropy

Although the evolution of anisotropy or distortional hardening is known to be pronounced in HCP materials (such as magnesium alloys in Ghaffari Tari *et al.*, 2014 and Abedini *et al.*, 2018a and titanium alloys in Gilles *et al.*, 2011 and Knezevic *et al.*, 2013), most commercial alloys exhibit some degree of evolving anisotropy with deformation. This implies that the shape of yield surface changes with deformation even under monotonic loading conditions due to evolution of materials crystallographic texture and consequently the yield stress ratios and r-values evolve with plastic strain.

Among the four materials studied in this paper, the evolution of anisotropy is expected to be insignificant for DP980, DP1180, and AA5182-O sheets. However, due to the features of the AA6063-T6 crystallographic texture described in Section 6.3, it is expected that this material undergoes a more significant plastic anisotropy evolution. In the present paper, the evolution of anisotropy was not considered; nevertheless, the approach can be effectively applied if progressively evolving yield surfaces are characterized as a function of plastic work

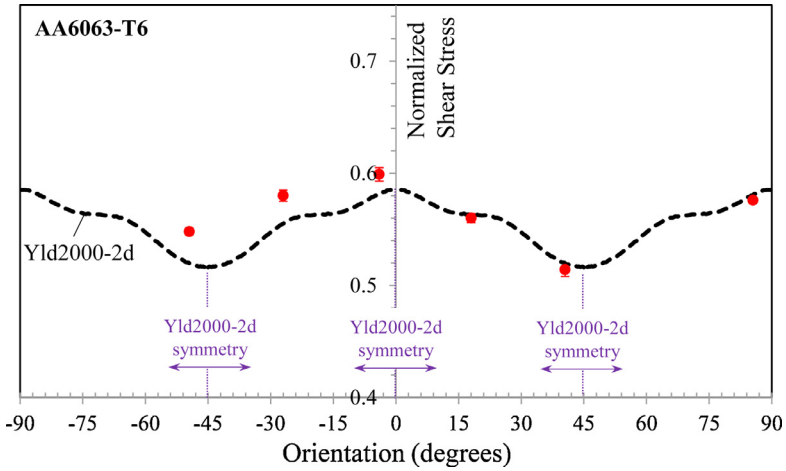

Figure. 14. Shear anisotropy of AA6063-T6 extrusion and prediction of the Yld2000-2d yield criterion with respect to the extrusion direction. Red symbols show the experimental data. The Yld2000-2d yield criterion is applicable for orthotropic-symmetric materials and has a symmetric response with a frequency of 45° in shear.

such that the instantaneous shear-to-tensile stress ratio can be derived with incremental deformation. In such a case, the variation of shear-to-tensile stress ratio arises from both evolution of anisotropy and rotation of the material frame; nonetheless, a unique solution can still be determined since these two effects are combined in the measurement.

7. Conclusions

In contrast to the classical uniaxial or biaxial tensile tests, simple shear tests remain free of plastic instabilities until much higher strains and provide a promising alternative to obtain the isotropic hardening response of materials. However, the rotation of the material axes with deformation and its interaction with shear anisotropy should be considered which is in general agreement with the observations of Chen *et al.* (2018) for torsion of tubes. To account for shear anisotropy and material frame rotation, the present study has investigated the mechanics of shear deformation of elastic-plastic materials. The following points summarize the main outcomes of this study:

- An experimental methodology was proposed to obtain the hardening response of materials using simple shear tests based upon plastic work equivalence while accounting for shear anisotropy and material frame rotation. This technique was employed to derive the hardening response of four different materials of DP980, DP1180, AA5182-O, and AA6063-T6.
- It was established that for relatively isotropic materials, such as the DP steels, accounting for material frame rotation may lead to relatively minor changes in the measured hardening curves. The influence of accounting for material frame rotation was found to be minor (on the order of 1.5% to 2%) for the two dual phase steels. The method of Rahmaan *et al.* (2017) that neglects the frame rotation is a reasonable approximation for materials with minor shear anisotropy.
- In contrast, accounting for material frame rotation on the hardening response of the aluminum alloys was significant with an increase of 5% for AA5182-O sheet and a decrease of 15% for AA6063-T6 extrusion.
- Normal stresses in simple shear for anisotropic materials in the *reference frame* are negligible on the order of 1% of the applied shear stress and should be equal in magnitude but opposite in sign.
- Artefacts in the calibration of associated anisotropic yield functions can cause erroneous normal stresses and the shear constraint of Abedini *et al.* (2018b) must be enforced for pressure-independent plasticity.
- Anisotropic yield functions can be calibrated with experimental shear data to provide a non-linear interpolation of the shear-to-tensile stress ratio. Anisotropic yield functions are restricted by convexity and are expected to provide a more robust approach for interpolation between the experimental shear stresses used in their calibration.
- Phenomenological interpolation functions can also be employed for the proposed shear conversion technique and comparable results to the non-linear interpolation using non-quadratic yield functions were obtained. This method is suggested when a full set of experimental data is not available to calibrate advanced anisotropic yield criteria.

Author Statement

N/A

Declaration of Competing Interest

The authors declare that they have no known competing financial interests or personal relationships that could have appeared to influence the work reported in this paper.

Acknowledgements

The authors would like to thank members of the Nonlinear Strain Path Project Team of the Auto/Steel Partnership (A/SP) for technical and financial support. The authors would like to acknowledge Amir Zhumagulov for his assistance with the shear tests as well as Professor Michael Worswick and Professor Kaan Inal of the University of Waterloo for valuable discussions on the constitutive characterization of materials.

References

Dunand, M, Mohr, D, 2010. Hybrid experimental-numerical analysis of basic ductile fracture experiments for sheet metals. International Journal of Solids and Structures 47, 1130–1143.
Tardif, N, Kyriakides, S, 2012. Determination of anisotropy and material hardening for aluminum sheet metal. International Journal of Solids and Structures 49, 3496–3506.
Roth C, C, Mohr, D, 2016. Ductile fracture experiments with locally proportional loading histories. International Journal of Plasticity 79, 328–354.
Abedini, A, Butcher, C, Worswick M, J, 2018a. Application of an evolving non-associative anisotropic-asymmetric plasticity model for a rare-earth magnesium alloy. Metals. https://doi.org/10.3390/met8182013.
Baral, M, Ha, J, Korkolis Y, P, 2019. Plasticity and ductile fracture modeling of an Al-Si-Mg die-cast alloy. International Journal of Fracture. https://doi.org/10.1007/s10704-019-00345-1.
Ha, J, Baral, M, Korkolis Y, P, 2019. Ductile fracture of an aluminum sheet under proportional loading. International Journal of Mechanics and Physics of Solids 132, 103685.
Coppieters, S, Cooreman, S, Sol, H, Van Houtte, P, Debruyne, D, 2011. Identification of the post-necking hardening behaviour of sheet metal by comparison of the internal and external work in the necking zone. International Journal of Materials Processing Technology 211, 545–552.
Rossi, M, Lattanzi, A, Barlat, F, 2018. A general linear method to evaluate the hardening behaviour of metals at large strain with full-field measurements. Strain. https://doi.org/10.1111/str.12265.
Flores, P, Tuninetti, V, Gilles, G, Gonry, P, Duchene, L, Habraken, A M, 2010. Accurate stress computation in plane strain tensile tests for sheet metal using experimental data. Journal of Materials Processing Technology 210, 1772–1779.
Koc, M, Billur, E, Cora O, N, 2011. An experimental study on the comparative assessment of hydraulic bulge test analysis and methods. Materials and Design 32, 272–281.
Hill, R, 1950. A theory of the plastic bulging of a metal diaphragm by lateral pressure. Philosophical Magazine 41, 1133–1142.
Mudler, J, Vegter, H, Aretz, H, Keller, S, van den Boogaard, A H, 2015. Accurate determination of flow curves using the bulge test with optical measuring systems. Journal of Material Processing Technology 226, 169–187.
Min, J, Stoughton T, B, Carsley J, E, Carlson, B, Lin, J, Gao, X, 2017. Accurate characterization of biaxial stress-strain response of sheet metal from bulge testing. International Journal of Plasticity 94, 192–213.
Peirs, J, Verleysen, P, Degrieck, J, 2012. Novel technique for static and dynamic shear testing of Ti6Al4V sheet. Experimental Mechanics 52, 729–741.
Yin, Q, Zillmann, B, Suttner, S, Gerstein, G, Biasutti, M, Tekkaya, A E, Wagner, M F X, Merklein, M, Schaper, M, Halle, T, Brosius, A, 2014. An experimental and numerical investigation of different shear tests configurations for sheet metal characterization. International Journal of Solids and Structures 51, 1066–1074.
Muhammad, W, Brahme, A, Kang, J, Mishra, R, Inal, K, 2017. Experimental and numerical investigation of texture evolution and the effects of intragranular backstresses in aluminum alloys subjected to large strain cyclic deformation. International Journal of Plasticity 93, 137–163.
Rahmaan, T, Abedini, A, Butcher, C, Pathak, N, Worswick M, J, 2017. Experimental investigation of strain rate effect on fracture characteristics of DP600 and AA5182-O sheet metal alloys under shear loading. International Journal of Impact Engineering 108, 303–321.
Abedini, A, Butcher, C, Worswick M, J, 2017a. Fracture characterization of rolled sheet alloys in shear loading: Studies of specimen geometries, anisotropy, and rate sensitivity. Experimental Mechanics 57, 75–88.
Abedini, A, Butcher, C, Rahmaan, T, Worswick M, J, 2018b. Evaluation and calibration of anisotropic yield criteria in shear loading: Constraints to eliminate numerical artefacts. International Journal of Solids and Structures 151, 118–134.
Traphöner, H, Heibel, S, Calusmeyer, T, Tekkaya, A E, 2018. Influence of manufacturing processes on material characterization with the grooved in-plane torsion tests. International Journal of Mechanical Sciences 146-147, 544–555.
Roth C, C, Mohr, D, 2018. Determining the strain to fracture for simple shear for a wide range of sheet metals. International Journal of Mechanical Sciences 149, 224–240.
Butcher, C, Abedini, A, 2017. Shear confusion: Identification of the appropriate equivalent strain in simple shear using logarithmic strain measure. International Journal of Mechanical Sciences 134, 273–283.
Noder, J, Butcher, C, 2019. A comparative investigation into the influence of the constitutive model on the prediction of in-plane formability for Nakazima and Marciniak tests. International Journal of Mechanical Sciences press.

Chen, K, Kyriakides, S, Scales, M, 2018. Effect of material frame rotation on hardening of an anisotropic material in simple shear tests. Journal of Applied Mechanics 85, 1–5.
Scales, M, Tardif, N, Kyriakides, S, 2016. Ductile failure of aluminum alloy tubes under combined torsion and tension. International Journal of Solids and Structures 97-98, 116–128.
Hill, R, 1948. A theory of the yielding and plastic flow of anisotropic metals, Proceeding of the Royal Society of London. Series A 193, 281–297.
Kohar, C, Bassani, J, Brahme, A, Muhammad, W, Mishra, R, Inal, K, 2019a. A new multiscale framework to incorporate microstructure evolution in phenomenological plasticity: Theory, explicit finite element formulation, implementation and validation. International Journal of Plasticity 117, 122–156.
Swift, H, 1947. Length changes in metals under torsional overstrain. Engineering 163, 253–257.
Xiao, H, 1997. Bruhns O T, Meyers A, Logarithmic strain, logarithmic spin and logarithmic rate. Acta Mechanica 124, 89–105.
Bruhns O, T, Xiao, H, Meyers, A, 1999. Self-consistent Eulerian rate type elasto-plasticity models based upon the logarithmic stress rate. International Journal of Plasticity 15, 479–520.
Barlat, F, Brem J, C, Yoon J, W, Chung, K, Dick R, E, Lege D, J, Pourboghrat, F, Choi S, H, Chu, E, 2003. Plane stress yield function for aluminum alloy sheets – part I: theory. International Journal of Plasticity 21, 1009–1039.
Butcher, C, Abedini, A, 2019. On anisotropic plasticity models using linear transformations on the deviatoric stress: Physical constraints on plastic flow in generalized plane strain. International Journal of Mechanical Sciences press.
Hosford, W, 1996. On the crystallographic basis of yield criteria. Texture Microstruct 26-24, 479–493.
Abedini, A, Butcher, C, Nemcko M, J, Kurukuri, S, Worswick M, J, 2017b. Constitutive characterization of a rare-earth magnesium alloy sheet (ZEK100-O) in shear loading: studies of anisotropy and rate sensitivity. International Journal of Mechanical Sciences 128-129, 54–69.
Chaboche J, L, 2008. A review of some plasticity and viscoplasticity constitutive theories. International Journal of Plasticity 24, 1642–1693.
Barlat, F, Gracio J, J, Lee, M, Rauch E, F, Vincze, G, 2011. An alternative to kinematic hardening in classical plasticity. International Journal of Plasticity 27, 1309–1327.
Rahmaan, T, Noder, J, Abedini, A, Zhou, P, Butcher, C, Worswick M, J, 2020. Anisotropic plasticity characterization of 6000- and 7000-series aluminum sheet alloys at various strain rates. International Journal of Impact Engineering 135, 103390.
Tian, H, Brownell, B, Baral, M, Korkolis Y, P, 2016. Earing in cup-drawing of anisotropic Al-6022-T4 sheet. International Journal of Material Forming. https://doi.org/10.1007/s12289-016-1282-y.
Ghaffari Tari, D, Worswick M, J, Ali, U, Gharghouri M, A, 2014. Mechanical response of AZ31B magnesium alloy: experimental characterization and material modeling considering proportional loading at room temperature. International Journal of Plasticity 55, 247–267.
Kohar, C, Zhumagulov, A, Brahme, A, Worswick, M, Mishra, R, Inal, K, 2016. Development of high crush efficient, extrudable aluminum front rails for vehicle lightweighting. International Journal of Impact Engineering 95, 17–34.
Zener, C, Hollomon J, H, 1944. Effect of strain rate upon plastic flow of steel. Journal of Applied Physics 15, 22–32.
Yin, Q, Soyarslan, C, Guner, A, Brosius, A, Tekkaya, A E, 2012. A cyclic twin bridge shear test for the identification of kinematic hardening parameters. International Journal of Mechanical Sciences 59, 31–43.
Muhammad, W, Ali, U, Brahme, A, Kang, J, Mishra, R, Inal, K, 2019. Experimental analyses and numerical modeling of texture evolution and the development of surface roughness during bending of an extruded aluminum alloy using a multiscale modeling framework. International Journal of Plasticity 117, 93–121.
Inal, K, Mishra, R, Cazacu, O, 2010. Forming simulation of aluminum sheets using an anisotropic yield function coupled with crystal plasticity theory. International Journal of Solids and Structures 47, 2223–2233.
Dumoulin, S, Engler, O, Hopperstad, O, Lademo, O, 2012. Description of plastic anisotropy in AA6063-T6 using the crystal plasticity finite element method. Modelling and Simulation of Materials Science and Engineering 20, 055008.
Kohar, C, Brahme, A, Hekmat, F, Mishra, R, Inal, K, 2019b. A computational mechanics engineering framework for predicting the axial crush response of aluminum extrusions. Thin-Walled Structures 140, 516–532.
Gilles, G, Hammami, W, Libertiaux, V, Cazacu, O, Yoon, J H, Kuwabara, T, Habraken, A M, Duchene, L, 2011. Experimental characterization and elasto-plastic modeling of the quasi-static mechanical response of TA-6 V at room temperature. International Journal of Solids and Structures 48, 1277–1289.
Knezevic, M, Lebensohn R, A, Cazacu, O, Revil-Baudard, B, Proust, G, Vogel S, C, Nixon M, E, 2013. Modeling bending of α-titanium with embedded polycrystal plasticity in implicit finite elements. Materials Science and Engineering A 564, 116–126.